

# A Finite Element Method for Cell Membranes with Tethered Obstacles

Christian Schmeiser<sup>a,b</sup>, Christoph B. Winkler<sup>b,1</sup>

<sup>a</sup> Faculty of Mathematics, University of Vienna, Oskar-Morgenstern-Platz 1, 1090 Vienna, Austria

<sup>b</sup> Johann Radon Institute for Computational and Applied Mathematics, Austrian Academy of Sciences, Apostelgasse 23, 1030 Vienna, Austria

<sup>1</sup> Corresponding author at: Johann Radon Institute for Computational and Applied Mathematics, Austrian Academy of Sciences, Apostelgasse 23, 1030 Vienna, Austria

*Email-address:* christoph.winkler@ricam.oeaw.ac.at

## Abstract

Simulation of cell membranes and whole cells has been performed with different approaches to explain various cellular shapes. An important, but often neglected, feature of this setting is the cytoskeleton, that acts as a set of dynamic point obstacles to the surface, which can also be tethered to it by breakable linkages. Due to the highly viscous cellular environment, a quasistatic model for the membrane is justified.

Based on previous work on the simulation of biological membranes, a framework to compute shape deformations under the influence of tethered point obstacles is established. First, the method is tested on a model problem with a membrane facing but a few impediments. The simulation model copes with large deformations and with the hysteresis effects caused by the breaking of tethers. Results of a realistic simulation of a lamellipodial frontal piece are presented with an account for the cytoskeleton's evolution and specific membrane proteins.

*Index Terms:* cell membrane, finite element, obstacle problem, tether

# 1 Introduction

We consider a parametrized, bounded and smooth surface in 3d that is periodic in the  $x$ -direction and has a given orientation. Generally the surface will resemble a bulged rectangle bent in the  $y - z$ -plane. The shape of the undisturbed surface is governed by the Helfrich energy [18], which reduces to the Willmore energy [35] (the surface integral over the squared mean curvature) due to prohibiting topological changes and the lack of a spontaneous curvature. On the inner side, the surface is constrained by an obstacle consisting of a set of dynamic points. These points are possibly tethered to the surface, with tethers pulling on the nearest location of the surface like springs, but only up to a maximal force. At the two boundaries not defined by the periodicity in the  $x$ -coordinate, a pulling force acts in the direction tangential to the surface. The last contribution to the model is an orthogonal force on the whole surface that pushes inside. The membrane shape is constrained by the conditions of the obstacle lying inside the surface, a fixed surface area and a regularity condition for the non-periodic boundary.

The membrane behaves in a quasistatic way to the moving obstacle. Specific difficulties for the surface description arise from the nonconvex energy contribution from the breakable tethers and the nonconservative pulling and volume forces. This leads to the formulation of a fixed point problem for the total energy conserved in the system.

The different parts of the formulated problem are related to well studied mathematical questions. First, there is the Willmore energy with its close connection to minimal surfaces [13]. The existence of minimizers to this energy has been studied in various settings [2, 23], especially for closed spheres of isoperimetric constraint [31, 19]. Secondly, the obstacle problem for mathematical membranes has been investigated thoroughly [6, 7]. Last, there are treatments of viscoelastic bodies that adhere to a foundation [8, 33]. Despite all these connections, the formulated problem does not fit either of the mentioned settings. In the treatment of the Willmore energy, mostly closed surfaces are regarded and no interaction with an obstacle occurs. Furthermore, in our setting without the obstacle a minimizer to the Willmore energy is easily constructed by just taking a rectangle lying in a plane. In the classical obstacle problem the membrane is captured with a governing equation that minimizes the surface length or area instead of the squared mean curvature. Thus the mathematical membrane behaves differently, from the point of view of the shape as well as analytically. And in the dealing with viscoelastic bodies there is obviously no membrane involved and the shape of the foundation is smooth. It seems that the stated problem has not yet been considered. The authors point out that no analytical results are presented in this work but a numerical method to capture the surface's behavior.

Numerous approaches have been used to numerically deal with deformable

surfaces that act under the influence of the Willmore energy (from now on called membranes). Phase field methods [14, 5], otherwise used for example in solidification dynamics, evolve one or more closed surfaces with the Willmore flow [22] and study their interaction. Surface finite elements are employed in [16] to describe the deformation and movement of whole biological cells and also describe the dynamics of mobile obstacles. Another finite element approach of high surface regularity is used in [17], which describes the isoperimetric deformation of a closed vesicle with a Loop subdivision surface [24]. The constructed surface is  $C^2$  and thus highly useful for the description of curvatures.

The presented approach transforms the constraints, especially the restrictions to the surface by the obstacle, via the penalty method into further contributions to the overall energy governing the surface. Time discretization allows to solve the fixed point problem with a gradient flow in each time step. To capture the membrane also a Loop subdivision surface is utilized, which in this setting can be simplified to describing the membrane with specific box splines [12]. The different boundaries have to be dealt with, with the one induced by the  $x$ -periodicity resulting in an identification of certain spline coefficients. Additional box splines along the freely deformable edges ensure the same regularity on the whole surface. To capture the membrane's shape with the highly deformable finite elements, a special surface integration technique is used. It takes into account the computational cost of additional splines while allowing a fine tuning of the surface to curvature and the obstacle. The force stemming from the obstacle is determined with a point-to-surface distance function that is an approximation of the Euclidean distance.

The motivation for this work is founded in cell biology [1], especially in the individual locomotion of cells. Lamellipodia [34] are the machinery for crawling of many different cell types (for a detailed introduction to the biological system and the modeling, the inclined reader is referred to the parallel publication [30]). These cell protrusions are flat but very wide sheets that are filled with an organized and ordered network of thin actin filaments [29] and enveloped by the cell membrane [15]. The meshwork is altered by the growth of filaments by polymerization of additional actin monomers, the creation of new filaments by branching from existing ones, untethering of filaments and subsequent capping that halts all processes for that filament [26]. The cross-linked filaments, that are anchored to the substrate, exert the driving force of the cell by growing in the direction of movement. The cell membrane is a lipid bilayer that acts like a two-dimensional fluid and deforms according to the Helfrich energy. The aim of this work is to compute how a cell membrane wraps around the tethered ends of the actin filaments. A follow up question, in detailed considered in [30], is concerned with the specific shape of lamellipodia. It is known that at their leading edge there are a number of membrane proteins that sense and/or create curvature in the

bilayer. But how they interact with the actin filaments is not yet established and especially why the lamellipodium keeps its peculiar aspect ratio has not been resolved so far.

The paper proceeds as follows: After defining the problem in a mathematically exact way in section 2, the numerical approach is presented in section 3. Section 4 contains simulation results, while section 5 further elaborates on the model and shows findings for full lamellipodia frontal pieces.

## 2 The mathematical membrane model

The modeled membrane, Fig. 1, lives in the domain  $\mathbb{T}^1 \times \mathbb{R}^2$ , with the one-dimensional torus  $\mathbb{T}^1$  given by the interval  $[0, L_1]$ . As  $L_1 = x_{max}$  is approximately the length of the leading edge and with a fixed membrane area of  $A_0$  (see below), the parameter space  $S = \mathbb{T}^1 \times [0, L_2]$  with  $L_2 = A_0/x_{max}$  is used for the parametrization

$$\mathcal{M}(t) = \{\mathbf{r}(\mathbf{s}, t) : \mathbf{s} \in S\} \subset \mathbb{T}^1 \times \mathbb{R}^2$$

of the membrane piece at time  $t \geq 0$ . The periodic nature of the membrane model is ensured by

$$\mathbf{r}(s_1 + L_1, s_2, t) = (r_1(\mathbf{s}, t) + x_{max}, r_2(\mathbf{s}, t), r_3(\mathbf{s}, t)).$$

The rear boundary  $\Gamma_r(t) := \mathbf{r}(\mathbb{T}^1 \times \{0, L_2\}, t)$  is built up by a bottom and a top part with  $s_2 = 0$  and, respectively,  $s_2 = L_2$ . In each simulation time step the membrane shape is ascertained as a local minimum of a potential energy functional.

### Contributions to the energy functional

We use an accustomed version of the Helfrich energy

$$E_{bend}[\mathcal{M}] := 2\mu_{bend} \int_{\mathcal{M}} H^2 d\sigma, \quad (1)$$

with the bending modulus  $\mu_{bend}$  to account for the bending of the membrane. The mean curvature  $H = \frac{k_1+k_2}{2}$  is derived from the principal curvatures  $k_1 \leq k_2$  (see Fig. 1.A). As irregularities of the membrane are described in the constraints, the cell membrane is assumed homogeneous in this formula.

The obstacle is a set of points  $\mathbf{F}_i(t)$ ,  $i \in I$ , representing barbed ends of actin filaments that are tethered to the membrane for  $i_t \in I_t \subseteq I$ . The tethers are modeled as springs,

$$E_{tether}(t)[\mathcal{M}] := \sum_{i \in I_t(t)} \min(\mu_{tether} d(\mathbf{F}_i(t), \mathcal{M})^2, \mathcal{F}_{max}^2), \quad (2)$$

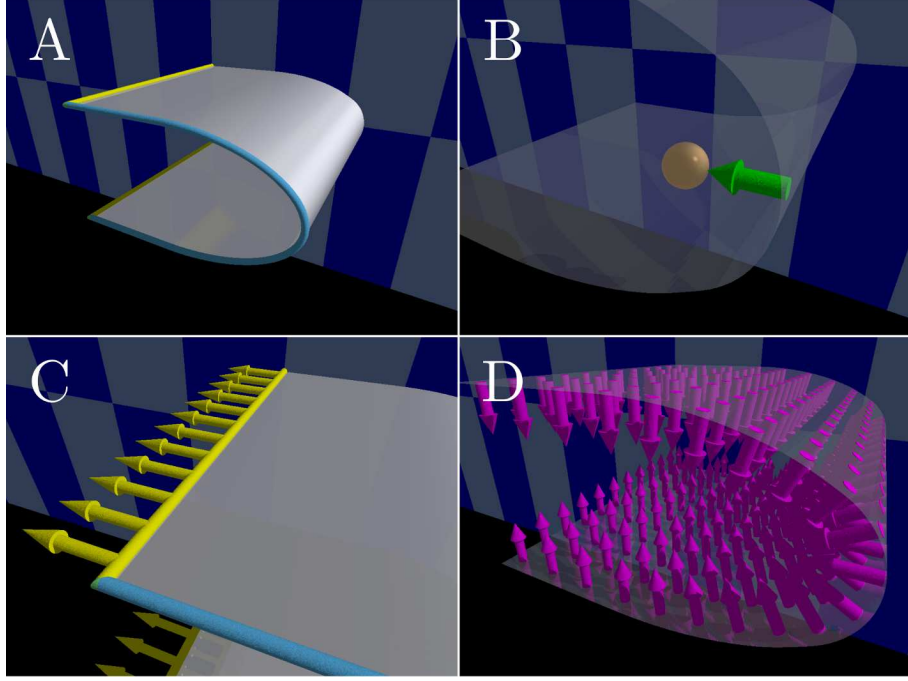


Figure 1: Schemes for different aspects influencing the membrane. A: Membrane scheme; the boundary  $\Gamma_r$  and the membrane at  $x_{max}$  are highlighted as yellow and, respectively, light blue tubes. The background wall functions as a reference only, with vertical stripes of width 100nm. B: Tether force; the linkage between the tethered obstacle (depicted in bronze) and the membrane (transparent) pulls at the membrane. This force is visualized by the green arrow. C: Stretching force; the stretching force (yellow) pulls at the membrane from behind. D: Volume constraint force; for  $\mu_{vol} > 0$  the inward pushing force (magenta) is acting on the whole membrane.

with a tether spring constant  $\mu_{tether}$  and the signed distance  $d(\mathbf{x}, \mathcal{M})$  giving the distance of a point  $\mathbf{x} \in \mathbb{R}^3$  to the membrane ( $d(\mathbf{x}, \mathcal{M}) > 0$  if  $\mathbf{x}$  is inside the cell), see Fig. 1.B. The levelling off at an maximal force of  $\mathcal{F}_{max}$  per tether makes the resulting energy nonconvex. This effect is balanced by the fact that tethers only sustain a maximal force of  $\mathcal{F}_{max}$  and break at higher strain.

Membrane tension leads to an energy contribution at the rear boundary:

$$E_{pull}(\mathcal{M}^*)[\mathcal{M}] := \mu_{pull} \int_{\Gamma_r^*} \mathbf{r} \cdot \mathbf{a}_n^* ds^*, \quad (3)$$

where  $ds$  is the length element along  $\partial\mathcal{M}$  and  $\mathbf{a}_n$  is the unit tangent vector of  $\mathcal{M}$  normal to  $\partial\mathcal{M}$  and oriented inwards, Fig. 1C. Quantities with the superscript  $*$  should not be seen as part of the argument  $\mathcal{M}$  of  $E_{pull}$ , although

they depend on the membrane deformation. This trick is used to formulate the energy contribution of the nonconservative pulling force.

A fixed total cell volume leads to the energy contribution

$$E_{vol}(\mathcal{M}^*)[\mathcal{M}] := \mu_{vol} \int_{\mathcal{M}^*} \mathbf{r} \cdot \mathbf{n}^* d\sigma^*, \quad (4)$$

with the unit outward (with respect to the cell) normal  $\mathbf{n}$  and the Lagrange multiplier  $\mu_{vol}$ , see Fig. 1.D. The meaning of the superscript  $*$  is as in (3) and likewise stems from the nonconservative nature of the force.

### Constraints

All barbed ends have to lie inside the cell

$$d(\mathbf{F}_i(t), \mathcal{M}(t)) \geq 0, \quad i \in I(t), \quad t \geq 0 \quad (5)$$

and the surface area is fixed:

$$\int_{\mathcal{M}(t)} d\sigma = \int_{\mathcal{M}(0)} d\sigma = A_0. \quad (6)$$

The rear boundary has to lie in a plane parallel to the  $x$ - and the  $z$ -axis:

$$\mathbf{r}_2(\mathbf{s}, t) = c(t), \quad \text{for } \mathbf{s} \in [0, L_1] \times \{0, L_2\}, c \in \mathbb{R}. \quad (7)$$

**The full membrane model:** With  $M(t)$ , the set of all admissible membrane shapes  $\mathcal{M}(t) = \mathbf{r}(S, t)$  meeting the constraints 5-7, the membrane's shape is a fixed point of the map  $\mathcal{M}^* \mapsto \mathcal{M}$ , defined by

$$\begin{aligned} \mathcal{M} &= \operatorname{argmin}_{\hat{\mathcal{M}} \in M(t)} E(\mathcal{M}^*, t)[\hat{\mathcal{M}}], \\ E(\mathcal{M}^*, t) &:= E_{bend} + E_{tether}(t) + E_{pull}(\mathcal{M}^*) + E_{vol}(\mathcal{M}^*). \end{aligned}$$

Since there is the possibility of more than one fixed point, it is also required that  $\mathcal{M}(t)$  should depend continuously on time, when this is true for  $E(\mathcal{M}^*, t)$ . In other words, the membrane's shape evolves according to a local minimum of  $E$ 's energy landscape as long as this landscape does not change drastically over time. Here, a drastic change can be caused by two events. First, the local minimum might disappear as eigenvalues of  $E$ 's linearization change their sign and make the minimum unstable. We assume only non-degenerate cases with just one eigenvalue becoming zero at a time. In such a case the membrane's shape is slightly disturbed with the according eigendirection projected to the manifold of admissible membrane shapes. The nearest local minimum is found by a gradient flow in the direction of  $-DE$ , the negative gradient of  $E$  in the manifold, until the next fixed point of  $\mathcal{M}^* \mapsto \mathcal{M}$ . Second, the ripping of tethers might drastically alter  $E$ 's energy landscape. Assuming the general case that  $\mathcal{M}^*$  is no extremum of the altered energy landscape, again the local minimum is attained by following  $-DE$ .

### 3 Numerical method

#### 3.1 Penalty method and time discretization

To solve the constrained problem of the plasma membrane shape we employ the well-known penalty method [10]. In this approach the side conditions are transformed into energy terms and incorporated into the initial equation, which leads to a high cost whenever the requirements are not satisfied. Since the side conditions are mostly equality constraints and in order to be consistent we use quadratic penalization in every term and do not resort to barrier functions [27].

**Penalty 1 – pushing filaments:** Filament ends sticking out of the membrane are penalized by the square of the barbed end’s distance:

$$P_{push}(t)[\mathcal{M}] := \mu_{push} \sum_{i \in I(t)} (d(\mathbf{F}_i(t), \mathcal{M}(t))_-)^2$$

**Penalty 2 – surface area:** The global area is enforced by weighting the cell membrane area’s deviation from the initial condition:

$$P_{area}[\mathcal{M}] := \mu_{area,g} \left( \int_{\mathcal{M}(t)} d\sigma - A_0 \right)^2$$

**Penalty 3 – rear boundary:** Deviations from the mean value of extension  $\mathfrak{d}_\eta$  in the direction of the  $y$ -axis

$$\mathfrak{d}_\eta := \frac{\int_{\Gamma_r} \mathbf{r}_2(\mathbf{s}, t) d\mathbf{s}}{\int_{\Gamma_r} d\mathbf{s}}$$

are penalized quadratically:

$$P_{rear}[\mathcal{M}] := \mu_{rear} \int_{\Gamma_r} (\mathbf{r}_2(\mathbf{s}, t) - \mathfrak{d}_\eta)^2 d\mathbf{s}$$

**The penalized membrane model** With these alterations the set of admissible functions  $M(t)$  becomes  $H^2(\Omega)$  and the membrane model reads:

$$\begin{aligned} \mathcal{M}(t) &= \operatorname{argmin}_{\hat{\mathcal{M}} \in M(t)} \mathcal{E}(\mathcal{M}^*, t)[\hat{\mathcal{M}}], \\ \mathcal{E}(\mathcal{M}^*, t) &:= E_{bend} + E_{tether}(t) + E_{pull}(\mathcal{M}^*) + E_{vol}(\mathcal{M}^*) + \dots \\ &\quad P_{push}(t) + P_{area} + P_{rear}. \end{aligned}$$

The discretization of time in steps of  $\Delta t$  makes it necessary to apply the above mentioned gradient flow adapted to  $\mathcal{E}$  in every time step. It is the authors’ hope that by increasing the penalty weights to infinity, the solution

of the penalized membrane model would converge to the original, constrained formulation. Such behavior was shown for several systems of equations [25, 4, 28], but here in this study no analysis in this respect was performed. We restrict ourselves to using big enough weights such that the system exhibits the desired restrictions to an visually acceptable degree. The gradient flow for  $\mathcal{E}$  itself is solved using a line search algorithm [3], starting from the shape of the previous time step  $\mathcal{M}(t - \Delta t)$  and evolving it according to  $-D\mathcal{E}$ . This procedure also guarantees to find a local minimum near the shape of the previous time step.

### 3.2 Finite elements

#### Box splines

The membrane  $\mathcal{M}(t)$  is represented with box splines [11, 12]. We give a short survey of basic properties that is modeled after the description in [20]. A box spline  $M_{\Xi}$  is a piecewise polynomial function with a finite support. It is uniquely constructed by an associated  $n \times m$  matrix  $\Xi$ , a multi-set of column directions in  $\mathbb{R}^n \setminus \{0\}$ . Assuming from now on that there is a subset of columns of  $\Xi$  that forms a basis of  $\mathbb{R}^n$ , the box spline  $M_{\Xi}$  centered at the origin can conveniently be constructed by inductive convolutions. To be specific, starting with

$$M_Z(\mathbf{x}) := \frac{1}{|\det(Z)|} \chi_Z(\mathbf{x}), \quad \mathbf{x} \in \mathbb{R}^n$$

for a submatrix  $Z$  of  $\Xi$  whose columns form a basis of  $\mathbb{R}^n$  and the characteristic function  $\chi_Z$  on the half-open parallelepiped  $Z[-1/2, 1/2)^n$ , the box spline  $M_{\Xi}$  is formed by iterative averaging and smoothening along the directions  $\xi$  in  $\Xi \setminus Z$  according to:

$$M_{Z \cup \xi}(\mathbf{x}) := \int_{-1/2}^{1/2} M_Z(\mathbf{x} - t\xi) dt, \quad \xi \in \mathbb{R}^n.$$

The resulting function is piecewise polynomial of at most degree  $\#\Xi - \dim \text{ran}(\Xi)$  over the support determined by the Minkowski sum of the columns of  $\Xi$ . The regularity of  $\Xi$  is  $C^{m(\Xi)-2}$ , with  $m(\Xi)$  the minimal number of columns of  $\Xi$  that have to be removed such that the remaining ones do not span  $\mathbb{R}^n$ .

Given a lattice  $GZ^n$  we can construct a  $C^{m(\Xi)-2}$  spline by summing shifted versions of the box spline  $M_{\Xi}$ :

$$\sum_{\mathbf{j} \in GZ^n} a(\mathbf{j}) M_{\Xi}(\mathbf{x} - \mathbf{j}),$$

Note that the resulting surface is in general not interpolating the values  $a(\mathbf{j})$ , but rather approximating them. Linear independence of the shifts  $M_{\Xi}(\mathbf{x} - \mathbf{j})$

and that they form a Riesz basis of the spanned spline space  $S_M$  holds iff

$$\det(Z) \in \{0, -\det G, \det G\}, \quad \forall Z \subseteq \Xi, Z \text{ is square.}$$

The space  $S_M$  can be characterized by the spaces  $\Pi_{m(\Xi)-1}$  of polynomials it includes and the space  $\Pi_{\#\Xi-\dim \text{ran}(\Xi)}$  it is included in,

$$\Pi_{m(\Xi)-1} \subseteq S_M \subseteq \Pi_{\#\Xi-\dim \text{ran}(\Xi)},$$

with  $\Pi_\alpha$  the polynomials of degree  $\leq \alpha$ .

### Membrane construction with box splines

The parameter space  $S$  is discretized with  $n_1$  and  $n_2$  points in the direction of  $s_1$  and  $s_2$ , respectively, starting in  $(0, 0)$ . The discretization step sizes,  $h_i := L_i/(n_i - 1)$  with  $i \in \{1, 2\}$ , define the  $2 \times 6$  matrix  $\Xi$ :

$$\Xi = \begin{bmatrix} h_1 & h_1 & 0 & 0 & h_1 & h_1 \\ 0 & 0 & h_2 & h_2 & h_2 & h_2 \end{bmatrix}$$

This results in a box spline  $M_\Xi : \mathbb{R}^2 \rightarrow \mathbb{R}$ , Fig. 2E, which is twice continuously differentiable and composed of at most quartic polynomials. It can be written as

$$M_\Xi(s_1, s_2) = \int_{-1}^1 (1 - |\tau|) \left(1 - \left|\frac{s_1}{h_1} - \tau\right|\right)_+ \left(1 - \left|\frac{s_2}{h_2} - \tau\right|\right)_+ d\tau$$

with a support given by the relation

$$\exists \tau \in [-1, 1] : \max \left\{ \left|\frac{s_1}{h_1} - \tau\right|, \left|\frac{s_2}{h_2} - \tau\right| \right\} \leq 1.$$

Inclined readers are referred to e.g. [36] for a list of the polynomials that build up the box spline.

The membrane  $\mathcal{M}(t)$  is constructed by the sum of  $n_1(n_2 + 2)$  linear independent, shifted versions of  $M_\Xi$ , each multiplied with a set of 3d coordinates  $\mathbf{x}(\mathbf{j}, t)$ , Fig. 3. Their centers are at

$$\begin{aligned} J &:= \{\mathbf{j} \in \mathbb{R}^2 \mid \mathbf{j}_i = j_i h_i, j_1 \in \{0, \dots, n_1 - 1\}, j_2 \in \{-1, \dots, n_2\}\} \subseteq G\mathbb{Z}^2 \\ G &:= \begin{bmatrix} h_1 & 0 \\ 0 & h_2 \end{bmatrix} \end{aligned}$$

Explicitly, the membrane reads:

$$\mathcal{M}(t) = \{\mathbf{r}(\mathbf{s}, t) \mid \mathbf{s} \in S\} = \left\{ \sum_{\mathbf{j} \in J} \mathbf{x}(\mathbf{j}, t) M_\Xi(\mathbf{s} - \mathbf{j}) \mid \mathbf{s} \in S \right\}$$

The boundaries of  $S$  are treated according to the appropriate behavior of the membrane. The periodicity condition in the direction of  $s_1$  is met by

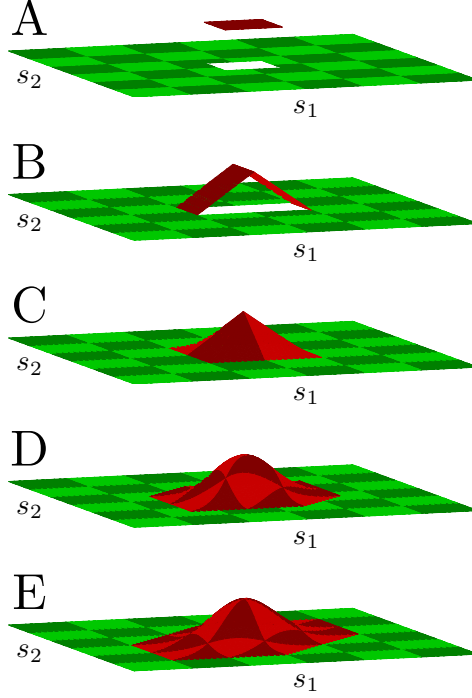


Figure 2: Schemes of box splines for  $h = h_1 = h_2$  with different scalings in height. Starting with  $\Xi = \begin{bmatrix} h & 0 \\ 0 & h \end{bmatrix}$  in A, each following picture shows the box spline with another direction added; B:  $\begin{bmatrix} h \\ 0 \end{bmatrix}$ , C:  $\begin{bmatrix} 0 \\ h \end{bmatrix}$ , D:  $\begin{bmatrix} h \\ h \end{bmatrix}$ , E:  $\begin{bmatrix} h \\ h \end{bmatrix}$ . The supports are depicted in red with the alternating color coding highlighting the different polynomial regions.

equating the coordinate values of the box splines that correspond to each other across  $s_1 \bmod L_1 = 0$

$$\mathbf{x}((n_1 - 1)h_1, \mathbf{j}_2, t) = \mathbf{x}(L_1, \mathbf{j}_2, t) = \mathbf{x}(0, \mathbf{j}_2, t) + [x_{max}, 0, 0],$$

and by adapting the box spline supports. In the direction of  $s_2$ , on the top and on bottom another row of box splines is set each, to ensure that the mapping of each pair  $(s_1, s_2) \in S$  is influenced by the same number of finite elements.

By representing the membrane  $\mathcal{M}(t)$  with the set of coordinates  $\mathbf{X}(t) := (\mathbf{x}(\mathbf{j}, t) | \mathbf{j} \in J) \in \mathbb{R}^{3n_1(n_2+2)}$ ,  $\mathcal{M}(t) = \mathcal{M}(\mathbf{X}(t))$ , the minimization problem of finding the best surface shape is transformed to identifying the optimal

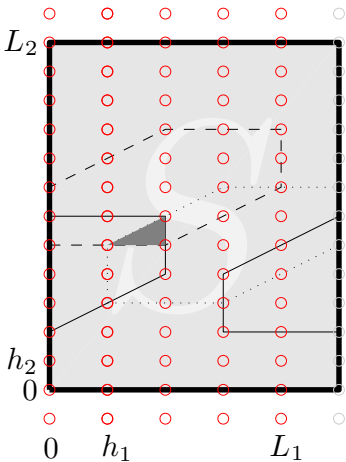


Figure 3: Scheme of the parameter space  $S$ . The positions of the box spline centers with free coordinates are highlighted in red, the other ones indicated as grey circles. The supports inside of  $S$  of three box splines is enframed with a solid, dashed or dotted line, respectively, and their intersection is depicted in dark grey. Note that the support of the box spline with the solid frame is on both side of  $s_1 \bmod L_1 = 0$ .

positions  $\mathbf{X}$ :

$$\mathcal{M}(\mathbf{X}(t)) = \operatorname{argmin}_{\widehat{\mathbf{X}} \in \mathbb{R}^{3n_1(n_2+2)}} \mathcal{E}(\mathcal{M}(\mathbf{X}^*), t)[\mathcal{M}(\widehat{\mathbf{X}})]$$

The constructed membrane fits the defining energy fine except at the points where the obstacle acts on. There the  $C^2$  regularity is too high and the obtained surface smoothens the solution. But given the rather smooth biological setting that motivates the whole model the chosen finite elements seen to be justified.

Curiously, the representation with the box spline  $M_{\Xi}$  is a special case of Loop subdivision surfaces [24]. The shifts of  $M_{\Xi}$  generate a tessallation  $\mathcal{T}$  of the parameter space  $S$  into the triangles  $\mathbf{e}$  defined by the supports of the piecewise polynomials (see Fig. 2 & 3). While in our representation all tessallation nodes have valence six, in general this condition is not required. This makes the method useful for shapes that cannot be approximated by rectangles, like spheres. The Loop subdivision scheme yields surfaces that are  $C^2$  except at irregular node points, where it is  $C^1$ . The representation with Loop subdivision surfaces was introduced to thin shells [9] and used in [17] to simulate closed biological cells.

The energy functionals and the penalization terms are adapted to the discretization of the membrane in a straightforward way. All the integrands of the energy contributions and the penalties are computed explicitly and not further discussed. The integration over the membrane surface has to be approximated numerically. First the computation over the whole membrane is broken down to the level of the mapped triangles  $\mathbf{t}_e(t) := \mathbf{r}(e, t)$ :

$$\int_{\mathcal{M}(t)} f d\sigma = \sum_{\mathbf{t}_e(t)} \int_{\mathbf{t}_e(t)} f d\sigma$$

Each triangle  $e \in \mathcal{T}$  itself is refined with smaller triangles of leg size  $h = \frac{1}{q}$  in barycentric coordinates  $\mathbf{v}$ , with  $q \in \mathbb{N}$ , see Fig. 4. Barycentric coordinates  $\mathbf{v} = (u, v, w)$  in triangles use linear combinations of the three vertices  $\{V_1, V_2, V_3\}$  to represent all interior and boundary points as  $uV_1 + vV_2 + wV_3$  with  $0 \leq (u, v, w) \leq 1$  and  $u + v + w = 1$ . Consequently the vertices of the refinement are

$$V = \{(hi, hj, 1 - h(i + j)) \mid (i, j) \in \{0, \dots, q\}^2, h(i + j) \leq 1\}$$

and the  $q^2$  centers of mass of the fine triangles follow as

$$C_m = \{(h(i + \frac{k}{3}), h(j + \frac{k}{3}), 1 - h(i + j + 2\frac{k}{3})) \mid (i, j) \in \{0, \dots, q\}^2, \dots, h(i + j + 2\frac{k}{3}) \leq 1, k \in \{1, 2\}\}.$$

For each triangle  $e$ , the refinement in the barycentric coordinates  $\mathbf{v}$  is

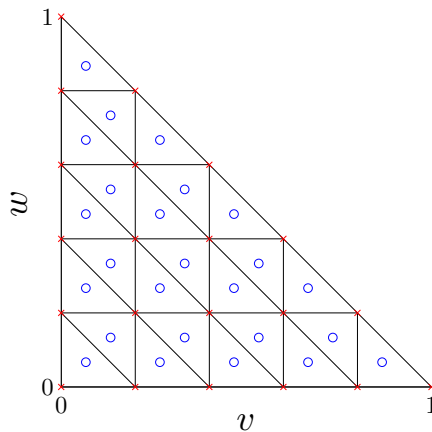


Figure 4: Scheme of the refinement in the barycentric coordinates  $v$  and  $w$ . The vertices  $V$  are highlighted in red, the centers of mass  $C_m$  in blue.

mapped to the parameter space  $S$

$$\mathbf{v} \mapsto \mathbf{s}_e(\mathbf{v}) \in \mathbf{e},$$

which leads with the definition of

$$\mathbf{r}_e(\mathbf{v}, t) := \mathbf{r}(\mathbf{s}_e(\mathbf{v}), t)$$

to the parametrization of the whole membrane  $\mathcal{M}(t)$  as:

$$\mathcal{M}(t) = \{\mathbf{r}_e(\mathbf{v}, t) | \mathbf{e} \in \mathcal{T}\}.$$

Finally, the surface integral is approximated by constant values over the fine triangulation and the surface area element  $\sqrt{a}(\mathbf{r})$ :

$$\begin{aligned} \int_{\mathcal{M}(t)} f d\sigma &= \sum_{\mathbf{t}_e(t)} \int_{\mathbf{t}_e(t)} f d\sigma \\ \int_{\mathbf{t}_e(t)} f d\sigma &\approx \frac{h^2}{2} \sum_{\mathbf{c}_m \in C_m} f(\mathbf{r}_e(\mathbf{c}_m, t)) \sqrt{a}(\mathbf{r}_e(\mathbf{c}_m, t)). \end{aligned}$$

This rather intricate procedure is utilized to combine the high deformability of the box splines with a rather low number of them, see Fig. 5. While the complexity of the minimization is kept low with rather few coordinate points  $\mathbf{x}$ , the membrane adapts well to the energy functional with a high number of evaluation points. The numbers  $n_i$  for the discretization of the parameter space  $S$  and  $q$  for the inner triangle refinement were determined heuristically and await further scrutiny.

To keep the overall membrane resolution roughly as in the initial setting, boundaries of the local area change are enforced with additional penalties,

$$\begin{aligned} P_{area,l,1}[\mathcal{M}] &= \mu_{area,l} \int_{\mathcal{M}(t)} \left( (\sqrt{a} - \alpha\sqrt{a_0})_- \right)^2 d\sigma \\ P_{area,l,2}[\mathcal{M}] &= \mu_{area,l} \int_{\mathcal{M}(t)} \left( (\sqrt{a} - \beta\sqrt{a_0})_+ \right)^2 d\sigma, \end{aligned}$$

with  $\alpha < 1$  and  $\beta > 1$ . The value  $\sqrt{a_0}$  may depend on  $\mathbf{s}$ , such that the membrane is locally more refined or less, see chapter 5. Note that this is done for reasons of numerical efficiency and stability only. A change of  $\sqrt{a_0}$  over time could account for better refinement depending on the local curvature of the membrane but has not been implemented. The value  $\mu_{area,l}$  is set such that this contribution has only very limited influence on the actual shape of the membrane.

Using the euclidean distance, the signed distance of a barbed end  $\mathbf{F}_i$  to a point  $\mathbf{r}(\mathbf{s})$  on the membrane  $\mathcal{M}$  becomes

$$d(\mathbf{F}_i(t), \mathbf{r}(\mathbf{s})) := \zeta \|\mathbf{F}_i(t) - \mathbf{r}(\mathbf{s})\|,$$

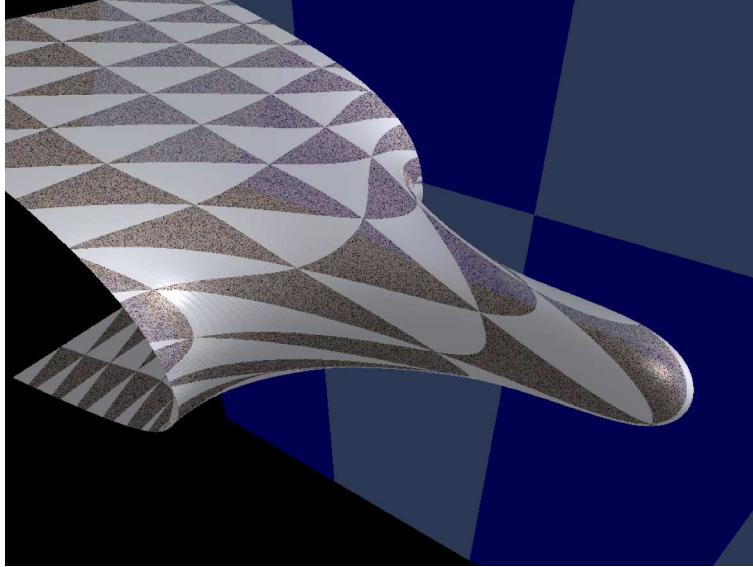


Figure 5: Deformability of the finite elements. Approximating the mapped triangles with plane ones without refinement would not capture the actual shape at the front of the dent.

with  $\zeta \in \{-1, 1\}$  indicating whether  $\mathbf{F}_i(t)$  lies inside the cell or not. So the minimal distance of a barbed end  $\mathbf{F}_i$  to the whole membrane  $\mathcal{M}$  becomes

$$d(\mathbf{F}_i(t), \mathcal{M}) := \zeta \min_{\mathbf{s} \in S} \|\mathbf{F}_i(t) - \mathbf{r}(\mathbf{s})\|,$$

An implementation of these two definitions would be time consuming. Already calculating the minimal distance of a barbed end  $\mathbf{F}_i$  to the image  $\mathbf{t}_e(t)$  of an element of the tessellation  $e \in \mathcal{T}$  by differentiating the square of the distance with respect to  $\mathbf{s}$ ,  $\frac{d d(\mathbf{F}_i(t), \mathbf{r}(\mathbf{s}, t))^2}{d\mathbf{s}}$ , and setting it to zero, results in a system of two fourth order polynomial equations for the barycentric coordinates.

To circumvent this challenge we approximate the distance by defining the signed distance of a barbed end  $\mathbf{F}_i(t)$  to a point on the membrane  $\mathbf{r}(\mathbf{s}, t)$  by its distance to the normal plane of the membrane in this point:

$$d(\mathbf{F}_i(t), \mathbf{r}(\mathbf{s}, t)) := (\mathbf{r}(\mathbf{s}, t) - \mathbf{F}_i(t)) \cdot \mathbf{n}(\mathbf{s}, t)$$

By using the fine grid

$$F := \bigcup_{e \in \mathcal{T}} \{\mathbf{r}_e(\mathbf{c}_m, t) | \mathbf{c}_m \in C_m\}$$

on  $\mathcal{M}(t)$  we define the distance of the barbed end to the membrane as

$$d(\mathbf{F}_i(t), \mathcal{M}(t)) := d(\mathbf{F}_i(t), \mathbf{r}_0),$$

with  $\mathbf{r}_0$  the element of  $F$  that minimizes  $\|\mathbf{F}_i(t) - \mathbf{r}_e(\mathbf{c}_m, t)\|$  for all elements in  $F$ . With this definition, the energies of the tethers and penalty 1 read

$$E_{tether}(t)[\mathcal{M}(\mathbf{X})] = \sum_{i \in I_t(t)} \min(\mu_{tether} d(\mathbf{F}_i(t), \mathcal{M}(\mathbf{X}))_+^2, \mathcal{F}_{max}^2)$$

$$P_{push}(t)[\mathcal{M}(\mathbf{X})] = \mu_{push} \sum_{i \in I(t)} (d(\mathbf{F}_i(t), \mathcal{M}(\mathbf{X}))_-)^2.$$

## 4 Numerical experiments

Numerical experiments have been performed to test the setting of the mathematical model and the feasibility of the implementation. The starting point of the time evolution is a membrane wrapped around five tethered obstacles, Fig. 6A. Four filament barbed ends are ordered around another one at  $[x_{max}/2, 0, 0]$ . The initial membrane shape already resembles the geometry of lamellipodial leading edges, as will be further discussed in the next section. The penalization parameters, Table 4, are not tuned to closely resemble a specific biological setting but to highlight the numerical method.

Symbol	Value
$\Delta t$	0.1s
$\mu_{push}$	$10^3$ pN/nm
$\mu_{area,g}$	$10^{-3}$ pN/nm <sup>-3</sup>
$\mu_{area,l}$	$10^{-3}$ pN/nm <sup>-3</sup>
$\mu_{rear}$	$10^2$ pN/nm <sup>2</sup>

Table 1: Weights of the penalizations for the numerical experiments

As time progresses, the central obstacle moves forwards and then backwards according to the velocity

$$v = \begin{cases} [0, 100, 0] & \text{for } 0 \leq t \leq 1 \\ [0, -100, 0] & \text{for } t \geq 1, \end{cases}$$

given in the dimensions of nm/s. The other barbed ends remain at their initial positions.

During the first second the protruding barbed end pushes the membrane forward in the middle and forms a bulge, Fig. 6B. Its creation is finished at time  $t = 1$ s with a shape that closely resembles a filopodium [32]. Notwithstanding the low number  $n_1$  of discretization points in  $s_1$ -direction, see Fig. 5, the dent is resolved in a smooth and symmetric way. Along with the middle barbed end the membrane retracts during the second second to its original position, although the values  $\mathbf{x}(\mathbf{j}, t)$  are altered, Fig. 6D. Further

pull-back leads to the formation of an invagination in the membrane's center that enlarges until the tether's breaking force is reached, Fig. 6E. The loss of the connection between the middle obstacle and the membrane immediately drastically changes the surface shape. A geometry similar to the initial condition is regained and this shows that the model is fully capable to capture hysteresis effects.

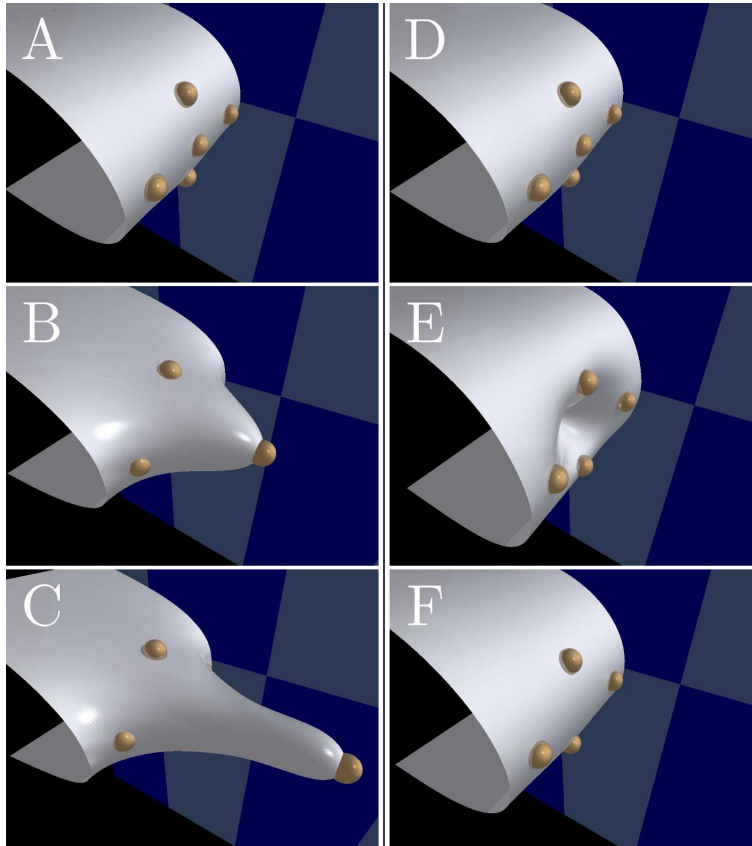


Figure 6: Numerical results: The left side shows the formation of the bulge at A: 0s, B: 0.5s and C: 1s. On the right side the invagination and ripping of the tether is visualized at D: 2s, E: 2.5s and F: 2.6s.

## 5 Full lamellipodium simulations

The membrane model is adapted to the very specific biological setting of lamellipodia leading edges, Fig. 7. There the geometric shape is influenced by special proteins that deform the membrane and simultaneously interact with the actin filament network. The simulation is furthermore enriched by a model for the evolution of the filaments.

## 5.1 Adaption of the leading edge

The leading edge is where the membrane is attached to a membrane protein cluster whose mechanical properties influence the membrane shape (see below). Describing its position in the parameter space by  $S_{\mathcal{L}} := \mathbb{T}^1 \times [L_2/2 - L/2, L_2/2 + L/2]$  leads to a leading edge of width  $L$ :

$$\mathcal{L}(t) := \{\mathbf{r}(\mathbf{s}, t) : \mathbf{s} \in S_{\mathcal{L}}\} \subset \mathcal{M}(t), \quad t \geq 0.$$

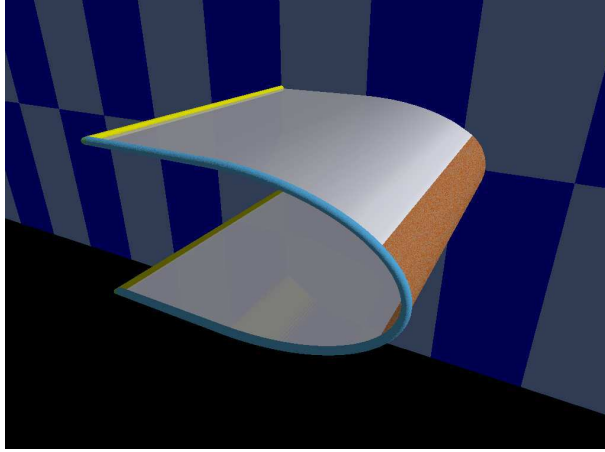


Figure 7: Scheme of the cell membrane with a densely packed protein cluster at the leading edge.

The specific nature of the aggregated membrane proteins at the leading edge motivates constraints on the shape and the width of the front section [30]

$$\mathbf{c}_2 \parallel \partial_{s_2} \mathbf{r}, \quad k_2 = \bar{\kappa}, \quad |\partial_{s_2} \mathbf{r}| = 1, \quad \text{for } s_2 \in [L_2/2 - L/2, L_2/2 + L/2], \quad (8)$$

$$\partial_{s_1}^2 \mathbf{r} \parallel \mathbf{n}, \quad \text{for } s_2 = L_2/2$$

The rear boundary has to lie in a plane defined by the  $x$ -axis and the vector  $\mathbf{d}(t) := (0, \cos(\omega(t)), \sin(\omega(t)))$ , which is orthogonal to the mean protrusion direction in the  $yz$ -plane since  $\omega$  is defined as the mean of the uncapped filament azimuth angles (see below):

$$\omega_i = \arcsin \left( \frac{f_{iz}}{\sqrt{f_{iy}^2 + f_{iz}^2}} \right), \quad i \in I_t(t) \cup I_u(t) \quad (9)$$

$$\mathbf{r}(\mathbf{s}, t) \cdot \mathbf{d}(t) = c(t), \quad \text{for } \mathbf{s} \in [0, L_1] \times \{0, L_2\}, c \in \mathbb{R}.$$

## Penalties

**Penalty 3 – rear boundary:** Deviations from the mean value of extension  $\mathfrak{d}$  in the direction of  $\mathbf{d}$

$$\mathfrak{d} := \frac{\int_{\Gamma_r} \mathbf{r}(\mathbf{s}, t) \cdot \mathbf{d} \, ds}{\int_{\Gamma_r} ds}$$

are penalized quadratically:

$$P_{rear}[\mathcal{M}] := \mu_{rear} \int_{\Gamma_r} (\mathbf{r}(\mathbf{s}, t) \cdot \mathbf{d} - \mathfrak{d})^2 \, ds$$

**Penalty 4 – leading edge:** The right description of the leading edge is facilitated by more than one energy contribution. First the inextensibility of the protein oligomers is dealt with by penalizing stretching or shrinking from the reference configuration:

$$P_{inex}[\mathcal{M}] := \mu_{inex} \int_{\mathcal{L}} (|\partial_{s_2} \mathbf{r}|^2 - 1)^2 \, d\sigma$$

Two energy contributions are used to ensure that the leading edge is bent with the IRSp53 bending radius  $\bar{\kappa}$ . By enforcing that the curvature on the membrane in the direction of  $s_2$  is  $\bar{\kappa}$

$$P_{le,bend}[\mathcal{M}] := \mu_{le,bend} \int_{\mathcal{L}} \left( \frac{\partial_{s_2 s_2} \mathbf{r} \cdot \mathbf{n}}{|\partial_{s_2} \mathbf{r}|^2} - \bar{\kappa} \right)^2 \, d\sigma$$

and weighting any deviation of the bigger main curvature  $k_1$  of the surface  $\mathcal{L}(t)$  from  $\bar{\kappa}$

$$P_{curv}[\mathcal{M}] := \mu_{curv} \int_{\mathcal{L}} (k_1 - \bar{\kappa})^2 \, d\sigma,$$

the resulting leading edge has the prescribed curvature property. Additionally this way the computation of the main curvature direction is not needed and especially its derivative according to membrane shape changes (see further down) is avoided. Last the symmetric bending of the oligomers is dealt with by making the second derivative of the leading edge middle position in  $s_1$  (the direction of change for the tangent vector in  $s_1$ ,  $\partial_{s_1 s_1} \mathbf{r}(s_1, L_{s_2}/2, t)$ ) point in the same direction as the membrane normal  $\mathbf{n}$ :

$$P_{sym}[\mathcal{M}] := \mu_{sym} \int_0^{x_{max}} ((\partial_{s_1 s_1} \mathbf{r} \cdot \mathbf{n})^2 - |\partial_{s_1 s_1} \mathbf{r}|^2) \, ds_1$$

Note that only the combination of all these penalties ensures that the leading edge's shape resembles the one biologically observed.

**Numerical lamellipodium model** Again the set of admissible functions  $M(t)$  is  $H^2(\Omega)$  and the lamellipodial membrane model is:

$$\begin{aligned} \mathcal{M}(\mathbf{X}(t)) &= \operatorname{argmin}_{\widehat{\mathbf{X}} \in \mathbb{R}^{3(n_1+2)(n_2+2)}} \mathcal{E}_{\mathcal{L}}(\mathcal{M}(\mathbf{X}^*), t) [\mathcal{M}(\widehat{\mathbf{X}})], \\ \mathcal{E}_{\mathcal{L}}(\mathcal{M}(\mathbf{X}^*), t) &:= E_{bend} + E_{tether}(t) + E_{pull}(\mathcal{M}(\mathbf{X}^*), t) + E_{vol}(\mathcal{M}(\mathbf{X}^*), t) + \dots \\ &\quad P_{push}(t) + P_{area} + P_{inex} + P_{bend} + P_{curv} + P_{sym} + P_{rear} + \dots \\ &\quad P_{area,l,1} + P_{area,l,2}. \end{aligned}$$

For the simulation of a whole lamellipodium the values of  $\sqrt{a_0}$  are chosen smaller in the front in bigger in the top and bottom rear parts. This reflects that there is a higher density of filament barbed ends in the IRSp53 cluster and a stronger curvature while relatively little is happening in the rather flat section towards the back.

Symbol	Value
$\mu_{push}$	1 pN/nm
$\mu_{area,g}$	$10^{-3}$ pN/nm <sup>-3</sup>
$\mu_{area,l}$	$10^{-7}$ pN/nm <sup>-3</sup>
$\mu_{inex}$	$3.5^{-4} \cdot 20\text{kbT}/\text{nm}^{-6}$
$\mu_{le,bend}$	$10^5$ pN nm
$\mu_{curv}$	$10^3$ pN nm
$\mu_{sym}$	$10^0$ pN/nm <sup>2</sup>
$\mu_{rear}$	$10^2$ pN/nm <sup>2</sup>

Table 2: Weights of the penalizations for the numerical treatment of a lamellipodial frontal piece.

## 5.2 Actin filaments

Actin filaments are modeled as oriented rods that are immobile and rigid. They are characterized by their barbed end position  $\mathbf{F}_i$ , their direction  $\mathbf{f}_i \in S^2$  and the indices  $i \in I(t) = \{1, \dots, N(t)\}$ .  $N(t) \in \mathbb{N}$  is the number of actin filaments and it is augmented by one at each branching event. Growth, nucleation of new filaments by branching, untethering and capping of filaments are included. Moreover there are three distinct sets of actin filaments, namely those that are tethered to the membrane,  $i \in I_t(t)$ , untethered,  $i \in I_u(t)$ , or capped,  $i \in I_c(t)$ . The polymerization rate of uncapped filaments  $i \in I_t(t) \cup I_u(t)$  is

$$k_p = \frac{k_{p,max}}{1 + \exp(\gamma(\mathcal{F}_i - \mathcal{F}_{stall}/2)\delta_i/k_B T)},$$

with the force  $\mathcal{F}_i$  acting between the filament end  $\mathbf{F}_i$  and the membrane  $\mathcal{M}(\mathbf{X}, t)$ , the shift  $\delta_i = l(\mathbf{n} \cdot \mathbf{f}_i)$  of the cell surface in the direction of the

normal  $\mathbf{n}$  and the thermal energy  $k_B T$ . The two parameters  $\mathcal{F}_{stall}$  and  $\gamma$  are chosen such that the maximal polymerization rate is reached up to a few percent for  $\mathcal{F}_i = 0$ , and that it is reduced to a few percent when  $\mathcal{F}_i = \mathcal{F}_{stall}$ . Branching occurs at a rate of

$$k_{br,i} = \frac{k_{br,max}}{1 + \rho_i L / n_{ref}},$$

with the maximal branching rate  $k_{br,max}$ , the local density of tethered barbed ends,  $\rho_i$ , and  $n_{ref}$  a reference barbed end number. The rather intricate determination of the branching direction involves several dependencies on the local geometry, deduced from the properties of the membrane protein IRSp53, and the interested reader is referred to the parallel modeling paper [30]. Tethers between the filament barbed ends and the membrane are either lost by a pulling force stronger than a critical value,  $\mathcal{F}_i = \mu_{tether} d(\mathbf{F}_i(t), \mathcal{M}(t)) > \mathcal{F}_{max}$ , or by a filament growing out of the leading edge region. Tethered filaments cannot form branches but keep on polymerizing. Additionally untethered filaments are susceptible to capping by a rate of  $p_{cap}$ , a process that completely stalls any further development. Periodic boundary conditions hold for the actin filaments in  $x$ -direction. As an initial condition for the actin filaments, the barbed ends  $\mathbf{F}_i(0)$  ( $i \in I_0 = \{1, \dots, N_0\}$ ) are placed on a surface resembling a typical lamellipodium shape with randomly distributed directions  $\mathbf{f}_i$ .

### Evolution of the filament meshwork

The processes altering the actin filament meshwork are implemented in straightforward ways. The growth by polymerization is implemented as an explicit Euler scheme, while branching and capping are modeled via the Monte Carlo method [21].

### Splitting

Although the lamellipodium in reality evolves as one system, it consists of two fundamentally distinct parts, namely the membrane and the actin filament network. We follow this distinction by splitting the numerical treatment into a section that adapts the membrane in a quasi-stationary way and another part that alters the meshwork. Since these two steps are alternated the influence of one part on the other, and thus the feedbacks of the sections on themselves, are kept.

## 5.3 Results for lamellipodia

Simulations show, see Fig. 8 and video in supporting material, that the method is able to cope with the membrane deformations typically found in

the evolution of lamellipodia. The surface reacts to the pushing and pulling forces by the actin filament barbed ends in a sensitive way and keeps the typical leading edge shape by preserving the IRSp53 band at the front. Most notably, we were able to reproduce the sustained lamellipodium flatness along with the determination of key characteristics of the actin filament network [30].

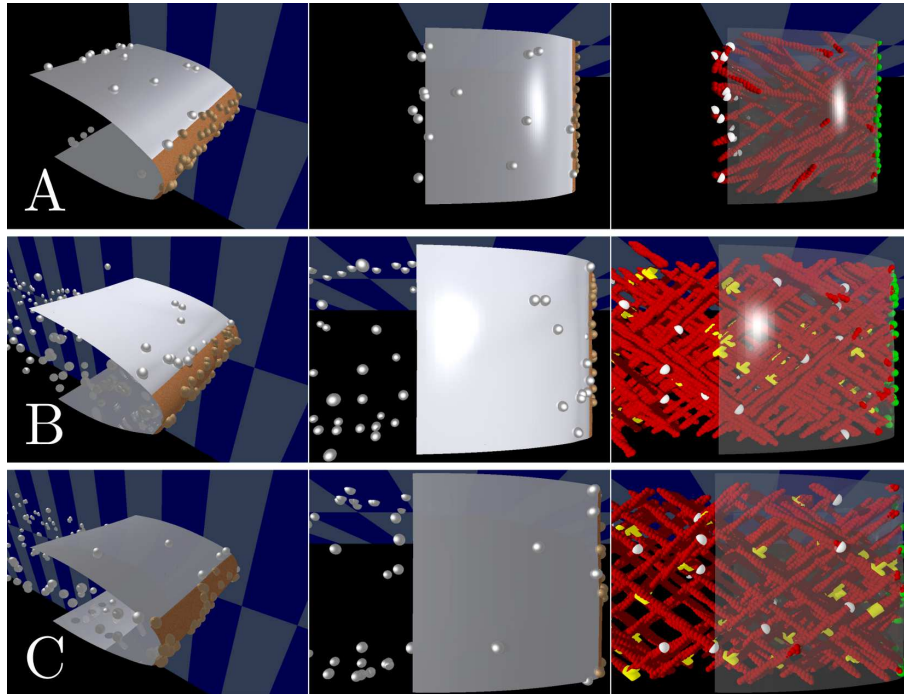


Figure 8: Time evolution of whole lamellipodium simulations after A: 0s, B: 60s and C: 120s from two different views. In the first two columns, tethered and untethered filament barbed ends are depicted as bronze and silver spheres, respectively. The membrane is shown in silver with the IRSp53 cluster highlighted in brown. The right column focuses on the actin filament network underlying the transparent membrane. The filaments are shown in red with tethered ends in green, white capped ones and branches are painted in yellow

## 6 Acknowledgements

This work has been supported by the Vienna Science and Technology Fund under grant no. MA09-004.

## References

- [1] B. Alberts, A. Johnson, J. Lewis, M. Raff, K. Roberts, and P. Walter. *Molecular Biology of the Cell*. Garland Science, New York, fourth edition, 2002.
- [2] M. Bauer and E. Kuwert. Existence of minimizing Willmore surfaces of prescribed genus. *Int. Math. Res. Notices*, 2003(10):553–576, 2003.
- [3] J. F. Bonnans, J. C. Gilbert, C. Lemaréchal, and C. A. Sagastizábal. *Numerical Optimization*. Springer, 2003.
- [4] C. Bost, G.-H. Cottet, and E. Maitre. Convergence analysis of a penalization method for the three-dimensional motion of a rigid body in an incompressible viscous fluid. *SIAM J. Numer. Anal.*, 48(4):1313–1337, 2010.
- [5] E. Bretin, Masnou S., and E. Oudet. Phase-field approximations of the Willmore functional and flow. *arXiv*, 0707.3168, 2013.
- [6] L. A. Caffarelli. The regularity of free boundaries in higher dimensions. *Acta Math.*, 139(1):155–184, 1977.
- [7] L.A. Caffarelli. *The obstacle problem*. Publications of the Scuola Normale Superiore. Scuola Normale Superiore, 1999.
- [8] O. Chau, M. Shillor, and M. Sofonea. Dynamic frictionless contact with adhesion. *ZAMP* 55, pages 32 – 47, 2004.
- [9] F. Cirak, M. Ortiz, and P. Schröder. Subdivision Surfaces: A New Paradigm For Thin-Shell Finite-Element Analysis. *Int. J. Numer. Meth. Eng.*, 47:2039–2072, 2000.
- [10] T. Courant. *Calculus of Variations and Supplementary Notes and Exercises*. New York University, 1962.
- [11] C. de Boor and R. DeVore. Approximation by smooth multivariate splines. *Trans. Amer. Math. Soc.*, 276:775 – 788, 1983.
- [12] C. de Boor, K. Höllig, and S. Riemenschneider. *Box Splines*. Applied Mathematical Sciences, 1993.
- [13] U. Dierkes, S. Hildebrandt, and F. Sauvigny. Minimal surfaces. In *Minimal Surfaces*, volume 339. Springer Berlin Heidelberg, 2010.
- [14] Q. Du, C. Liu, and X. Wang. A phase field approach in the numerical study of the elastic bending energy for vesicle membranes. *J. Comput. Phys.*, 198(2):450–468, 2004.

- [15] M. Edidin. Lipids on the frontier: a century of cell-membrane bilayers. *Nat. Rev. Mol. Cell Biol.*, 4:414–418, 2003.
- [16] C.M. Elliott, B. Stinner, and C. Venkataraman. Modelling cell motility and chemotaxis with evolving surface finite elements. *J. R. Soc. Interface*, 9(30):3027 – 3044, 2012.
- [17] F. Feng and W.S. Klug. Finite element modeling of lipid bilayer membranes. *J. Comput. Phys.*, 220:394–408, 2006.
- [18] W. Helfrich. Elastic Properties of Lipid Bilayers: Theory and Possible Experiments. *Z. Naturforsch. C*, 28:693–703, 1973.
- [19] L. G. A. Keller, A. Mondino, and T. Riviere. Embedded Surfaces of Arbitrary Genus Minimizing the Willmore Energy Under Isoperimetric Constraint. *Arch. Ration. Mech. An.*, 212(2):645–682, 2014.
- [20] Minho Kim. Quartic Box-Spline Reconstruction on the BCC Lattice. *IEEE T. Vis. Comput. Gr.*, 19(2):319–330, Feb 2013.
- [21] D. P. Kroese, T. Taimre, and Z.I. Botev. *Handbook of Monte Carlo Methods*. John Wiley & Sons, 2011.
- [22] Ernst Kuwert and Reiner Schätzle. The Willmore Flow with Small Initial Energy. *J. Differ. Geom.*, 57(3):409–441, 03 2001.
- [23] Ernst Kuwert and Reiner Schätzle. Minimizers of the Willmore functional under fixed conformal class. *J. Differ. Geom.*, 93(3):471–530, 03 2013.
- [24] C. Loop. Smooth Subdivision Surfaces Based on Triangles. Master’s thesis, 1987.
- [25] D. G. Luenberger. Convergence Rate of a Penalty-Function Scheme. *J. Optimiz. Theory App.*, 7(1), 1971.
- [26] J. Müller. Baculovirus-induced Actin Comet Tails: Structure of the Propulsion Machinery. Master’s thesis, 2012.
- [27] J. Nocedal and S. Wright. *Numerical Optimization*. Springer, 1999.
- [28] D. Oelz. Convergence of the penalty method applied to a constrained curve straightening flow. *Comm. in Math. Sciences*, 12(4):601–621, 2014.
- [29] T. D. Pollard and J. A. Cooper. Actin, a Central Player in Cell Shape and Movement. *Science*, 326(5957):1208–1212, 2009.

- [30] C. Schmeiser and C. B. Winkler. The Flatness of Lamellipodia Explained by the Interaction Between Actin Dynamics and Membrane Deformation. To be submitted soon.
- [31] Johannes Schygulla. Willmore Minimizers with Prescribed Isoperimetric Ratio. *Arch. Ration. Mech. An.*, 203(3):901–941, 2012.
- [32] J.V. Small and K.R. Rottner. *Actin-based Motility*, chapter Elementary Cellular Processes Driven by Actin Assembly: Lamellipodia and Filopodia, pages 3–33. Springer Science, 2010.
- [33] A. Touzaline. Study of a viscoelastic frictional contact problem with adhesion. *Comment. Math. Univ. Carolin.*, 52(2):257–272, 2011.
- [34] G. van Meer, D. R. Voelker, and G. W. Feigenson. Membrane lipids: where they are and how they behave. *Nat. Rev. Mol. Cell Biol.*, 9:112–124, 2008.
- [35] T. J. Willmore. *Riemannian Geometry*. Oxford University Press, 1996.
- [36] X.-M. Zeng, G.-R. Zhou, and L.-Q. Yang. Best bounds on the distance between 3-direction quartic box spline surface and its control net. *Appl. Math. J. Chinese Univ.*, 28(2):147–157, 2013.